Computational aspects of simulating wind induced ovalling vibrations in silo groups

J. Hillewaere[a,*], J. Degroote[b], G. Lombaert[a], J. Vierendeels[b], G. Degrande[a]

[a] *Department of Civil Engineering, KU Leuven, Kasteelpark Arenberg 40, B-3001 Leuven, Belgium*
[b] *Department of Flow, Heat and Combustion Mechanics, Ghent University, St.Pietersnieuwstraat 41, B-9000 Ghent, Belgium*

Abstract

During a storm in October 2002, wind induced ovalling vibrations were observed on several empty silos of a closely spaced group of 8 by 5 thin-walled silos in the port of Antwerp (Belgium). To determine realistic dynamic wind loads and hence clarify the cause of the wind induced ovalling vibrations in the silo group, 2D URANS simulations are performed for 7 angles of incidence between 0° and 90°. The emphasis in this paper is on the extensive verification and validation of the simulations to ascertain the accuracy of the numerical results. Subsequent analysis of the fluctuating wind pressures on the silo surfaces shows that ovalling oscillations of the eigenmodes with three and four circumferential wavelengths will be induced at the lee side of the silo group, corresponding with the lowest structural eigenfrequencies of the silos and the pattern of the visually detected vibrations during the 2002 storm.

Keywords: wind induced vibrations, ovalling, accuracy, grid refinement, time step refinement

1. Introduction and motivation

During a storm in October 2002, ovalling was observed on several empty silos near the corners of a group of 40 silos in the port of Antwerp (Belgium). Wind induced ovalling vibrations are an aeroelastic phenomenon where the cross section of the structure deforms as a shell without bending deformation with respect to the longitudinal axis of symmetry [1]. While realistic information on dynamic wind loads is increasingly important to improve the design of such flexible structures, it is difficult to obtain reliable design pressures. Design codes, e.g. Eurocode 1 [2], typically provide only basic quasi-static wind pressures for a restricted class of structures with a simple geometry. To clarify the cause and the location of the wind induced ovalling vibrations in the silo group, organized in 5 rows of 8 silos (figure 1), computational fluid dynamics (CFD) simulations are hence an interesting alternative to more expensive wind tunnel tests or in situ measurements to determine the transient wind loads on the silo structures.

The observed structural behaviour of the silos during the storm and the ovalling mode shapes and according natural frequencies of the silos are presented first. The numerical simulations of the turbulent wind flow, modelled as incompressible (low Mach number) flow, around the Antwerp silo group are the topic of the third section. After a thorough description of the applied computational procedure, the verification of the simulations through grid and time step refinement is discussed. Since no experimental data are available for the present closely spaced group configuration (pitch-to-diameter ratio of 1.05) in a storm regime at post-critical Reynolds number ($\mathrm{Re} = 1.24 \times 10^7$), validation of the simulations is not trivial. First, the numerical procedure is validated for the better documented case of 2D flow around a single cylinder in post-critical

*Corresponding author. Tel.: +32 16 32 16 77; fax: +32 16 32 19 88.
Email address: jeroen.hillewaere@bwk.kuleuven.be (J. Hillewaere)
URL: http://www.kuleuven.be/bwm (J. Hillewaere)

Postprint submitted to Journal of Computational and Applied Mathematics
Published version: J. Hillewaere, J. Degroote, G. Lombaert, J. Vierendeels, and G. Degrande. Computational aspects of simulating wind induced ovalling vibrations in silo groups. *Journal of Computational and Applied Mathematics*, 246:161–173, 2013. http://dx.doi.org/10.1016/j.cam.2012.06.033

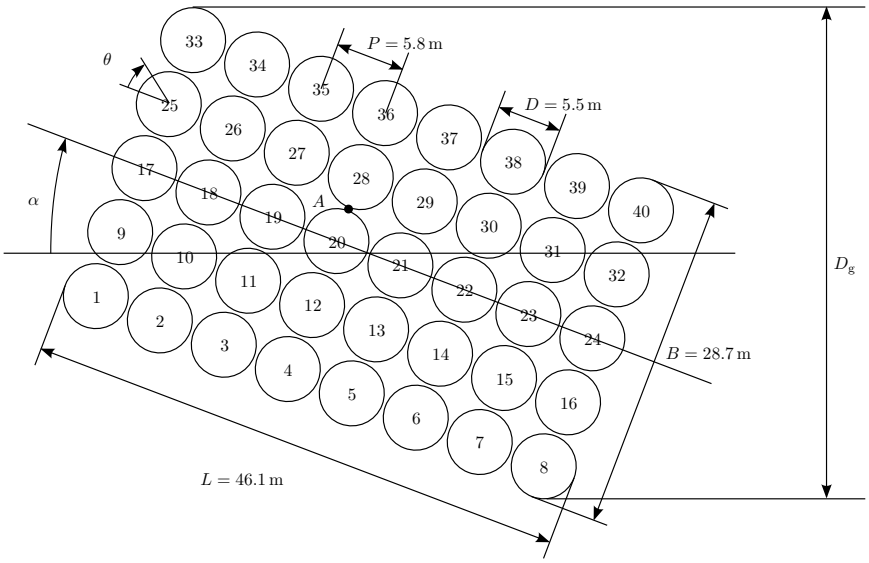

Figure 1: Plan view of the silo group with numbering of the invididual silos. Dimensions are given as well as definitions for the angle of incidence α and the angle θ on the circumference of an individual cylinder.

regime. Subsequently, the even more challenging simulations of the 2D flow around the entire silo group are also validated qualitatively by assessing similarities with the flow within tube arrays (e.g. heat exchangers) and the flow around rectangular cylinders. In the last section, the transient pressure distribution on the silo walls is investigated to verify whether and at which locations in the group pressure fluctuations can excite the ovalling eigenmodes of the silos. The influence of the angle of incidence α of the wind flow on these results is investigated while other parameters such as spacing ratio, Reynolds number, etc. are left unchanged.

2. Observations and structural properties of the silo group

The ovalling mode shapes for the present thin walled empty silos (diameter $D = 5.5\,\mathrm{m}$ and wall thickness $\mathrm{t} = 0.07\,\mathrm{m} - 0.10\,\mathrm{m}$ varying along the height of the silo) have been studied by Dooms et al. [3] and are referred to by a couple (m, n) where m denotes the half wave number in the axial direction and n is the number of circumferential waves (figure 2). The lowest natural frequencies f_n for these silos are found for ovalling mode shapes $(1, 3)$ and $(1, 4)$ both at $f_\mathrm{n} = 3.93\,\mathrm{Hz}$.

During the storm in October 2002, ovalling was observed on several silos near the lee side corner of the silo group (i.e. silo 40 and neighbouring silos 24, 32, 38, 39, etc.). The visually detected pattern of oscillations seems to have excited ovalling mode shapes $(1, 3)$ and $(1, 4)$. Since the specific atmospheric conditions near the silo group were not monitored during the storm, approximative wind conditions are set up, based on the location of the group and design wind velocities for storm conditions in Eurocode 1 [2]. A mean wind velocity $v_\infty = 31.8\,\mathrm{m/s}$ is found at half the height of the silos, resulting in a post-critical wind flow at Reynolds number $\mathrm{Re} = v_\infty D/\nu = 1.24 \times 10^7$. The global wind direction at the time of ovalling was at an angle of incidence of approximately $\alpha = 30°$ (figure 1).

3. Numerical simulations of the air flow around the silo group

The turbulent air flow around the 8 by 5 silo group is simulated for 7 angles of incidence α between 0° and 90°, leaving other influencing parameters unchanged (e.g. spacing ratio, Reynolds number, etc.). To ascertain the accuracy of the numerical results, extensive verification and validation have to be performed. It is first thoroughly verified whether the numerical results are independent of grid size and time step.

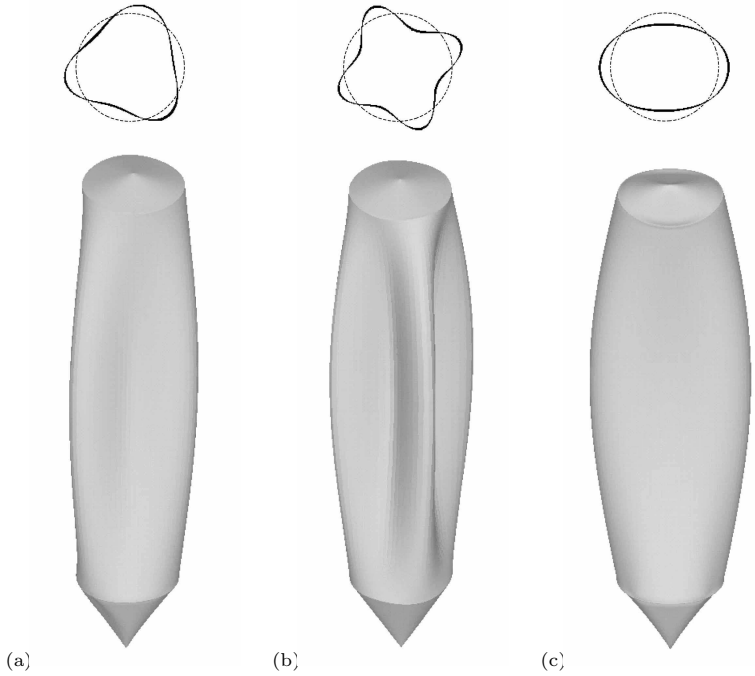

Figure 2: Selected ovalling eigenmodes of a single silo, (a) mode $(1, 3)$ at 3.93 Hz, (b) mode $(1, 4)$ also at 3.93 Hz and (c) mode $(1, 2)$ at 7.75 Hz [3].

Subsequently, the results should ideally be validated with results from wind tunnel experiments or on site measurements. Since no experimental data or comparable numerical data are available, other approaches have to be followed to validate the numerical model. First, the better documented case of 2D flow around a single cylinder in the post-critical regime is validated using the identical numerical procedure and boundary conditions as for the entire silo group simulations. Afterwards, a qualitative validation is performed by comparing the flow phenomena with the geometrically similar flow within tube arrays (e.g. heat exchangers) and the flow around rectangular cylinders. A distinction is hence implicitly made between vibrations related to the periodicity of the interstitial flow and vibrations caused by the large vortex structures behind the entire cylinder bundle.

3.1. Computational procedure

The 2D unsteady Reynolds averaged Navier-Stokes (URANS) discretized set of equations is solved in the Ansys FLUENT software package, using the hybrid shear-stress transport (SST) turbulence model. While 3D flow simulations over complex bodies have become possible in recent years, they remain very expensive and are therefore limited to moderate Reynolds numbers. On the contrary, 2D simulations are quite feasible, even for complex geometries and relatively high Reynolds numbers. Moreover, while the flow around the entire silo group and in its wake is clearly 3D, the smaller scale flow phenomena near the lee side corner silos are much more 2D. A coupled pressure-based calculation with a second order interpolation of the pressure, a second order upwind interpolation of momentum, turbulent kinetic energy k and specific dissipation rate ω is performed, while a second order implicit, unconditionally stable, time stepping method is used.

In the computations, the air density is $\rho = 1.25\,\mathrm{kg/m^3}$ and its dynamic viscosity is $\mu = 1.76 \times 10^{-5}\,\mathrm{Pa\,s}$. For the single cylinder simulations, the boundaries of the rectangular computational domain are placed at distances of $9D$ from the cylinder center for the inlet and the lateral boundaries and $30D$ for the outlet of the domain, with D the diameter of the cylinder. Equivalently, $9D_\mathrm{g}$ and $30D_\mathrm{g}$ are used for the group configuration, with D_g the projected width of the silo group (figure 1). At the velocity inlet, mean free stream velocity $v_\infty = 31.8\,\mathrm{m/s}$ and reasonably low turbulence intensity Tu = 1% and turbulence length

scale $l = 1.8\,\mathrm{m}$ are applied. Imposing higher turbulence intensities in URANS simulations increases the turbulence viscosity of the incident flow and yields unphysical results, altering for instance corner silo drag and lift coefficients as shown in respectively figures 3c and 4c for Tu = 10%. For Tu = 0.1% (figures 3a and 4a) and Tu = 1% (figures 3b and 4b), similar time histories of drag and lift coefficients are found and the incident flow does not act as a numerically much more viscous fluid. This is also reflected quantitatively in the mean and root mean square (r.m.s.) values of the drag coefficient ($\overline{C_d}$ resp. $C_{d,rms}$, table 1) and lift coefficient ($\overline{C_l}$ resp. $C_{l,rms}$, table 2). Values for Tu = 0.1% and Tu = 1% are similar while for Tu = 10%, $\overline{C_d}$ and $C_{d,rms}$ are significantly lower for all corner silos and $C_{l,rms}$ clearly deviates for e.g. silos 8 and 40. Figure 4 confirms that the mean lift coefficients are predicted rather accurately for Tu = 10% but amplitudes of fluctuations are clearly underestimated. These observations justify the application of Tu = 1% at the inlet of the domain for URANS simulations. While the higher turbulence intensities associated with larger length scales are typically expected in atmospheric boundary layer flows (e.g. values up to Tu = 20% [4]), these yield unphysical results in the 2D URANS simulations since large turbulence length scales should be resolved and not modelled. However, in 2D one can not represent these large length scales in a correct way, so it is better to disregard them since they will not interact with the much smaller scale silo structures. The outlet boundary is modelled as a pressure outlet with static pressure equal to the reference pressure. At the lateral boundaries symmetry is imposed. The cylinder walls are considered smooth and no-slip boundary conditions are applied.

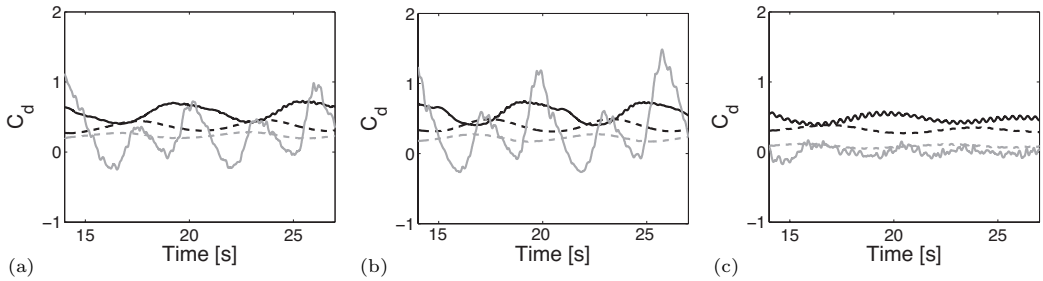

Figure 3: Time history of drag coefficient for the corner silos of the 8 by 5 silo group (silo 1 - dashed black line; silo 8 - solid black line; silo 33 - dashed grey line; silo 40 - solid gray line) with wind flow at angle of incidence $\alpha = 30°$ and for inlet turbulence intensity (a) Tu = 0.1%, (b) Tu = 1% and (c) Tu = 10%.

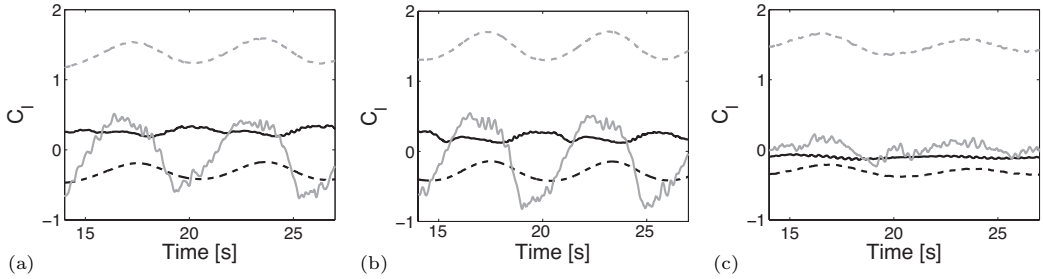

Figure 4: Time history of lift coefficient for the corner silos of the 8 by 5 silo group (silo 1 - dashed black line; silo 8 - solid black line; silo 33 - dashed grey line; silo 40 - solid gray line) with wind flow at angle of incidence $\alpha = 30°$ and for inlet turbulence intensity (a) Tu = 0.1%, (b) Tu = 1% and (c) Tu = 10%.

3.2. Verification of the computational procedure

To guarantee the accuracy of the results, it is required to verify the numerical procedure. Some of the most important results and conclusions of both grid and time step refinement studies are mentioned in the following.

	Tu = 0.1%		Tu = 1%		Tu = 10%	
	$\overline{C_d}$	$C_{d,rms}$	$\overline{C_d}$	$C_{d,rms}$	$\overline{C_d}$	$C_{d,rms}$
silo 1	0.371	0.375	0.397	0.402	0.326	0.328
silo 8	0.561	0.570	0.599	0.610	0.471	0.474
silo 33	0.237	0.239	0.218	0.221	0.086	0.089
silo 40	0.229	0.382	0.363	0.560	0.002	0.066

Table 1: Mean value and root mean square value of drag coefficient for the corner silos of the 8 by 5 silo group with wind flow at angle of incidence $\alpha = 30°$ and for inlet turbulence intensity Tu = 0.1%, Tu = 1% and Tu = 10%.

	Tu = 0.1%		Tu = 1%		Tu = 10%	
	$\overline{C_l}$	$C_{l,rms}$	$\overline{C_l}$	$C_{l,rms}$	$\overline{C_l}$	$C_{l,rms}$
silo 1	-0.309	0.322	-0.294	0.311	-0.303	0.307
silo 8	0.259	0.262	0.201	0.207	-0.104	0.105
silo 33	1.392	1.397	1.486	1.493	1.503	1.506
silo 40	-0.012	0.672	-0.126	0.467	0.020	0.096

Table 2: Mean value and root mean square value of lift coefficient for the corner silos of the 8 by 5 silo group with wind flow at angle of incidence $\alpha = 30°$ and for inlet turbulence intensity Tu = 0.1%, Tu = 1% and Tu = 10%.

3.2.1. Time step refinement

The determination of the time step to be applied in all the simulations is very important since a too large time step size will yield inaccurate results while an excessively small time step is computationally inefficient. Several time step refinements were performed for the present simulations. For the two smallest time steps that were considered, the time history of drag and lift coefficient of the corner silos of the silo group are shown in figures 5 and 6 while mean and r.m.s. values of drag and lift are given in tables 3 and 4 respectively. It is observed that the results of the simulations with the larger time step $\Delta t = 0.005\,\mathrm{s}$ are nearly identical to the results of the four times smaller time step $\Delta t = 0.00125\,\mathrm{s}$. Thus, $\Delta t = 0.005\,\mathrm{s}$ is applied in all simulations.

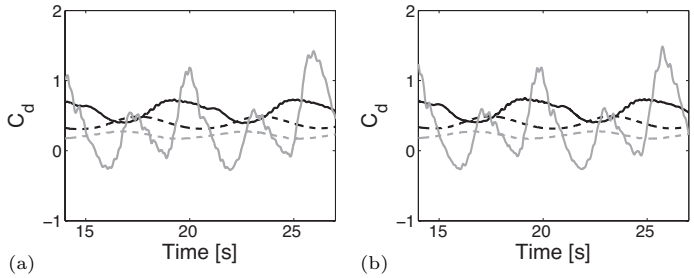

Figure 5: Time history of drag coefficient for the corner silos of the 8 by 5 silo group (silo 1 - dashed black line; silo 8 - solid black line; silo 33 - dashed grey line; silo 40 - solid gray line) with wind flow at angle of incidence $\alpha = 30°$ and for time step size (a) $\Delta t = 0.00125\,\mathrm{s}$ and (b) $\Delta t = 0.005\,\mathrm{s}$.

	$\Delta t = 0.00125\,\mathrm{s}$		$\Delta t = 0.005\,\mathrm{s}$	
	$\overline{C_d}$	$C_{d,rms}$	$\overline{C_d}$	$C_{d,rms}$
silo 1	0.388	0.393	0.397	0.402
silo 8	0.586	0.596	0.599	0.610
silo 33	0.218	0.221	0.218	0.221
silo 40	0.333	0.547	0.363	0.560

Table 3: Mean value and root mean square value of drag coefficient for the corner silos of the 8 by 5 silo group with wind flow at angle of incidence $\alpha = 30°$ and for time step size $\Delta t = 0.00125\,\mathrm{s}$ and $\Delta t = 0.005\,\mathrm{s}$.

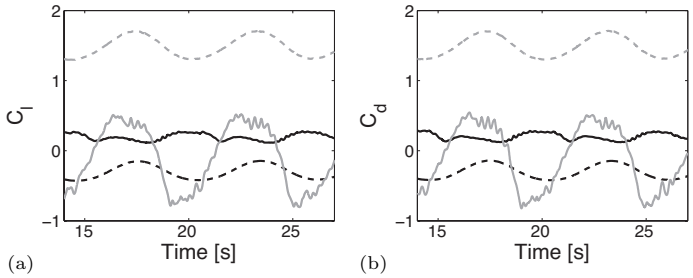

Figure 6: Time history of lift coefficient for the corner silos of the 8 by 5 silo group (silo 1 - dashed black line; silo 8 - solid black line; silo 33 - dashed grey line; silo 40 - solid gray line) with wind flow at angle of incidence $\alpha = 30°$ and for time step size (a) $\Delta t = 0.00125\,\mathrm{s}$ and (b) $\Delta t = 0.005\,\mathrm{s}$.

	$\Delta t = 0.00125\,\mathrm{s}$		$\Delta t = 0.005\,\mathrm{s}$	
	$\overline{C_l}$	$C_{l,rms}$	$\overline{C_l}$	$C_{l,rms}$
silo 1	-0.306	0.320	-0.294	0.311
silo 8	0.195	0.201	0.201	0.207
silo 33	1.477	1.483	1.486	1.493
silo 40	-0.118	0.461	-0.126	0.467

Table 4: Mean value and root mean square value of lift coefficient for the corner silos of the 8 by 5 silo group with wind flow at angle of incidence $\alpha = 30°$ and for time step size $\Delta t = 0.00125\,\mathrm{s}$ and $\Delta t = 0.005\,\mathrm{s}$.

3.2.2. Grid refinement

Similarly as for the time step refinement, the computational mesh was refined in several stages to determine the optimal mesh resolution. One particular, very important issue in this context is the refinement of the near-wall region which has an influence on the prediction of the dynamic pressures on the cylinder surface. A detail of the computational mesh in vicinity of the walls of the cylinders is shown in figure 7. A structured rectangular grid was generated around each of the cylinders while in the far field, an unstructured triangular mesh is applied. The grid size in the unstructured mesh in the far field gradually increases towards the boundaries of the computational domain, where accuracy is less important.

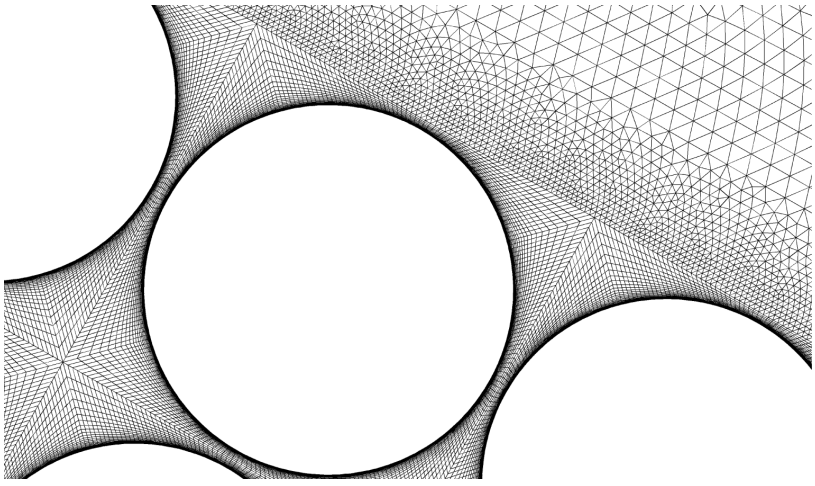

Figure 7: Detail of the computational grid for the 8 by 5 cylinder group in vicinity of the cylinder walls.

Drag and lift coefficients of the corner silos are compared for four levels of near-wall grid refinement in figures 8 and 9, clearly illustrating the different RANS near-wall modelling techniques. For a constant number of cells along the circumference of the cylinder surface, the aspect ratio (AR) of the wall-adjacent

grid cells affects the dimensionless distance to the wall $y^+ = v_\tau y/\nu$ and the dimensionless velocity v^+, with $v_\tau = \sqrt{\tau_w/\rho}$, y the distance to the wall and τ_w the wall shear stress. For $y^+_{max} = 196$ (AR = 25, figures 8a and 9a) and for $y^+_{max} = 102$ (AR = 50, figures 8b and 9b), the first grid point in the near wall region is located in the log-law region ($50 < y^+ < 500$) and logarithmic wall functions are used to model the boundary layer. For $y^+_{max} = 50$ (AR = 98, figures 8c and 9c), by contrast, the first grid point is located in the buffer layer of the boundary layer ($5 < y^+ < 50$). A hybrid technique applying either the log-law wall functions that are only valid in the log-law region or the linear (laminar) functions that are only applicable in the viscous sublayer of the boundary layer is then used, yielding inaccurate results. Increasing the aspect ratio even further to AR = 600 (figures 8d and 9d), the linear behaviour of the laminar viscous sublayer ($y^+ \approx 1$) is resolved in the simulation. However, values of $y^+_{max} = 11$ for this very fine near-wall grid are still slightly too large and hence, not all wall-adjacent cells are in the viscous sublayer. Nevertheless, it can be observed in figures 8 and 9 that the behaviour of drag and lift are similar in all simulations, except for the case when the first grid point is located in the buffer layer ($y^+_{max} = 50$) and the near wall flow is modelled inaccurately. This is confirmed by comparing numerical values for mean and r.m.s. values of drag and lift coefficients in tables 5 and 6. Especially for the silo at the lee side corner of the group (silo 40), root mean square values of drag and lift are significantly smaller when the wall adjacent cell is in the buffer layer ($y^+_{max} = 50$). Since the computational effort for a grid extending into the viscous sublayer for all elements along the wall would become prohibitively large, the simulations will be performed using the less time consuming wall functions with the first grid point in the log-law region ($y^+_{max} = 102$).

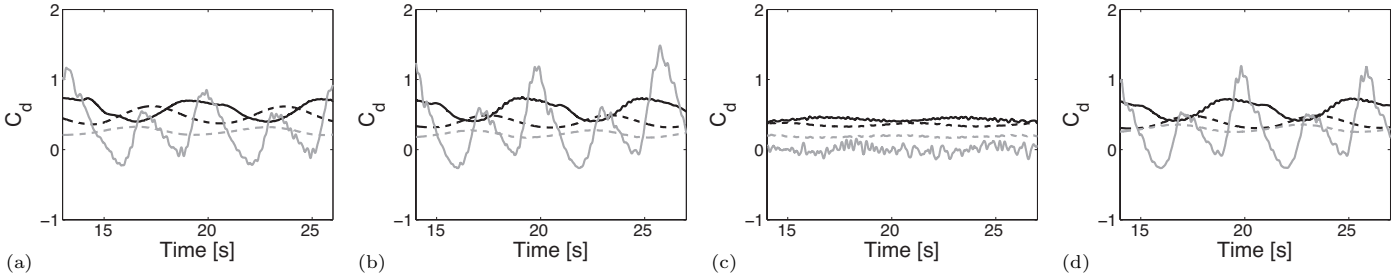

Figure 8: Time history of drag coefficient for the corner silos of the 8 by 5 silo group (silo 1 - dashed black line; silo 8 - solid black line; silo 33 - dashed grey line; silo 40 - solid gray line) with wind flow at angle of incidence $\alpha = 30°$ and for different near wall refinements: (a) $y^+_{max} = 196$, AR = 25, (b) $y^+_{max} = 102$, AR = 50, (c) $y^+_{max} = 50$, AR = 98 and (d) $y^+_{max} = 11$, AR = 600.

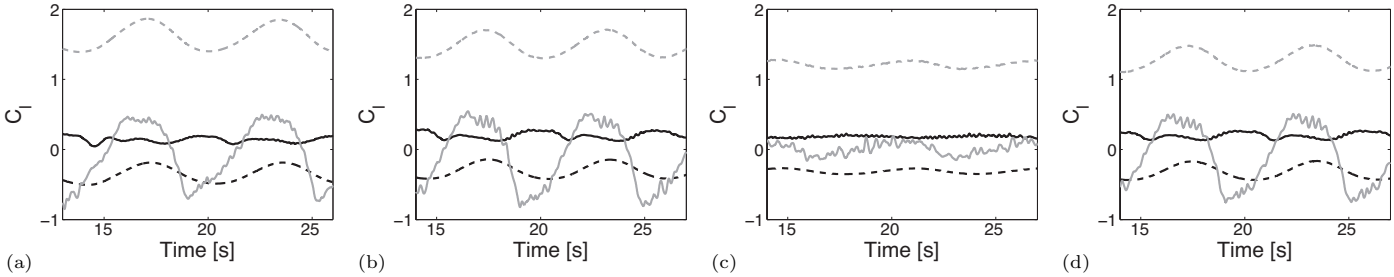

Figure 9: Time history of lift coefficient for the corner silos of the 8 by 5 silo group (silo 1 - dashed black line; silo 8 - solid black line; silo 33 - dashed grey line; silo 40 - solid gray line) with wind flow at angle of incidence $\alpha = 30°$ and for different near wall refinements: (a) $y^+_{max} = 196$, AR = 25, (b) $y^+_{max} = 102$, AR = 50, (c) $y^+_{max} = 50$, AR = 98 and (d) $y^+_{max} = 11$, AR = 600.

3.3. Validation of single cylinder simulations

The Building Block Approach, introduced by the AIAA [5], allows for the validation of a proposed computational procedure with a simpler sub-system for which experimental data are available. The lack of

	$y^+_{max} = 196$		$y^+_{max} = 102$		$y^+_{max} = 50$		$y^+_{max} = 11$	
	$\overline{C_d}$	$C_{d,rms}$	$\overline{C_d}$	$C_{d,rms}$	$\overline{C_d}$	$C_{d,rms}$	$\overline{C_d}$	$C_{d,rms}$
silo 1	0.495	0.503	0.397	0.402	0.355	0.356	0.379	0.383
silo 8	0.551	0.561	0.599	0.610	0.429	0.429	0.577	0.587
silo 33	0.271	0.274	0.218	0.221	0.188	0.189	0.298	0.300
silo 40	0.219	0.354	0.363	0.560	-0.002	0.058	0.250	0.426

Table 5: Mean value and root mean square value of drag coefficient for the corner silos of the 8 by 5 silo group with wind flow at angle of incidence $\alpha = 30°$ and for different near wall refinements: $y^+_{max} = 196$, $y^+_{max} = 102$, $y^+_{max} = 50$ and $y^+_{max} = 11$.

	$y^+_{max} = 196$		$y^+_{max} = 102$		$y^+_{max} = 50$		$y^+_{max} = 11$	
	$\overline{C_l}$	$C_{l,rms}$	$\overline{C_l}$	$C_{l,rms}$	$\overline{C_l}$	$C_{l,rms}$	$\overline{C_l}$	$C_{l,rms}$
silo 1	-0.337	0.355	-0.294	0.311	-0.308	0.310	-0.321	0.333
silo 8	0.128	0.133	0.201	0.207	0.181	0.182	0.193	0.197
silo 33	1.635	1.643	1.486	1.493	1.215	1.216	1.268	1.274
silo 40	0.040	0.365	-0.126	0.467	0.014	0.092	-0.063	0.410

Table 6: Mean value and root mean square value of lift coefficient for the corner silos of the 8 by 5 silo group with wind flow at angle of incidence $\alpha = 30°$ and for different near wall refinements: $y^+_{max} = 196$, $y^+_{max} = 102$, $y^+_{max} = 50$ and $y^+_{max} = 11$.

experimental data for the 8 by 5 silo group makes this approach particularly appealing and the numerical procedure is validated for the flow around a single cylinder.

The present numerical results are compared with experimental data and results of other (2D and 3D) numerical simulations. Several parameters are compared: the separation angle θ_s (figure 10), the pressure coefficient and the Strouhal number $\mathrm{St} = f_{vs}L/v_\infty$, with f_{vs} the vortex shedding frequency, v_∞ the free stream velocity of the fluid and L the characteristic length, equal to the diameter D of the cylinder in the present case. The pressure coefficient $C_p(\theta, t)$ along the circumference of a cylinder at a certain time t is defined as

$$C_p(\theta, t) = \frac{p(\theta, t) - p_\infty}{\rho v_\infty^2/2} \tag{1}$$

with p_∞ the free stream pressure. The time averaged pressure coefficient $\overline{C}_p(\theta)$ is calculated over multiple vortex shedding periods. The time averaged pressure coefficient for the present, single cylinder simulation is shown in figure 10 with $\theta_s = 116°$ and $\mathrm{St} = 0.32$.

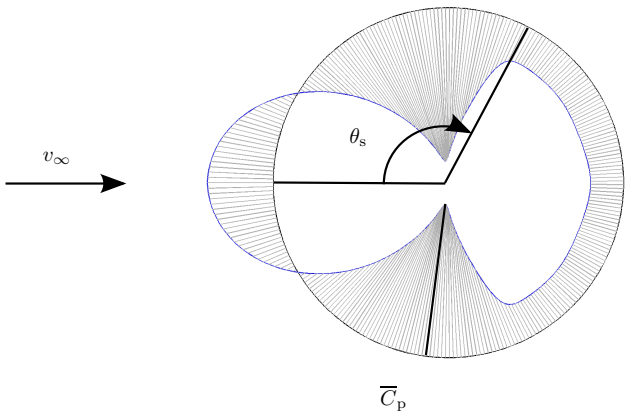

Figure 10: Time averaged pressure coefficient $\overline{C}_p(\theta)$ on the circumference of the cylinder with indication of the free stream velocity v_∞ and the separation angle θ_s.

Experimental data for high Reynolds number flows around circular cylinders are only scarsely available in literature, e.g. Shih et al. [6] give experimental pressure coefficients at $\mathrm{Re} = 0.8 \times 10^7$ (figure 11).

Zdravkovich [7] gives an elaborate overview of experimental results at Reynolds numbers from 0.73×10^7 to 3.65×10^7 (figure 11) where separation occurs between $\theta_s = 100°$ and 110°. For Reynolds numbers larger than 0.5×10^7, experimental smooth flow data of Zan [8] indicate that the Strouhal number remains at 0.2, whereas Schewe [9] found that it rises to about 0.3 as the Reynolds number approaches a value of 10^7; consistent with the tendency of the Strouhal number to rise from 0.2 to 0.3 in the range of Reynolds numbers between 10^6 and 10^7 [7].

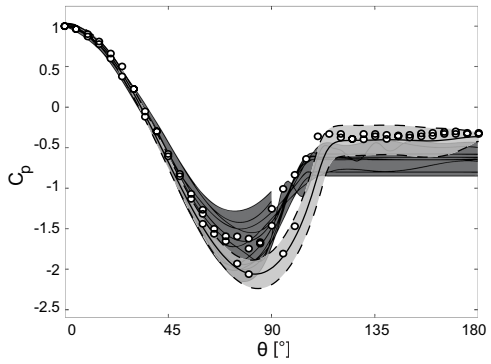

Figure 11: Comparison of the present calculated maximal, minimal (dashed lines) and time averaged pressure coefficients $\overline{C}_p(\theta)$ (solid line) for the flow around a single cylinder at $\mathrm{Re} = 1.24 \times 10^7$ with experimental results of Zdravkovich [7] for $0.73 \times 10^7 \leq \mathrm{Re} \leq 3.65 \times 10^7$ (dark grey zone) and Shih et al. [6] at $\mathrm{Re} = 0.8 \times 10^7$ (○).

Several numerical simulations have been reported in the literature for highly turbulent cross flows around circular cylinders. Younis and Przulj [10] performed 2D URANS simulations at $\mathrm{Re} = 0.35 \times 10^7$ with different turbulence models and report a Strouhal number of 0.28 and separation at $\theta_s = 120°$. Travin et al. [11] applied 3D DES for Reynolds numbers up to 3×10^6 and found a Strouhal number 0.35 with separation at $\theta_s = 111°$.

In view of the considerable scatter on the experimental and numerical data from literature due to differences in Reynolds number, applied turbulence model, etc., reasonable agreement is found between the present simulations ($\mathrm{St} = 0.32$, $\theta_s = 116°$) and the data from literature.

3.4. Qualitative validation of silo group simulations

Apart from validating the computational procedure for the single cylinder case, the numerical results can only be validated qualitatively by comparing the present physical flow phenomena with similar, well documented flow applications. The flow around bluff, rectangular cylinders is considered to assess the flow around the silo group while the flow through tube bundles (e.g. in heat exchangers) is compared with the flow in the interstitial spaces of the group. However, these applications should be considered as a step towards a better understanding of the physical phenomena dominating the flow around the silo group by highlighting similarities and discrepancies rather than data the present results should perfectly match.

3.4.1. The flow around the cylinder group

At the transverse corner cylinders of the group (e.g. cylinders 8 and 33 for $\alpha = 30°$, see figure 12c), shear layers in the outer flow are separated while approximately 10% of the flow is forced through the interstitial spaces in the group. These interstitial flows emerge at the lee side, join up and form several local recirculation zones in the wake that coalesce as they are carried downstream. One large scale vortex street is formed in the wake of the entire group, with a flow periodicity depicted by the Strouhal number St (table 7) with characteristic length $L = D_g$. For the smallest angles of incidence ($\alpha = 0°$ and 15°, figures 12a and 12b), it is clear that the emerging interstitial flows on the upper downstream side of the group (cylinders 33 to 40) are joined up and dragged downstream without forming local recirculation zones, due

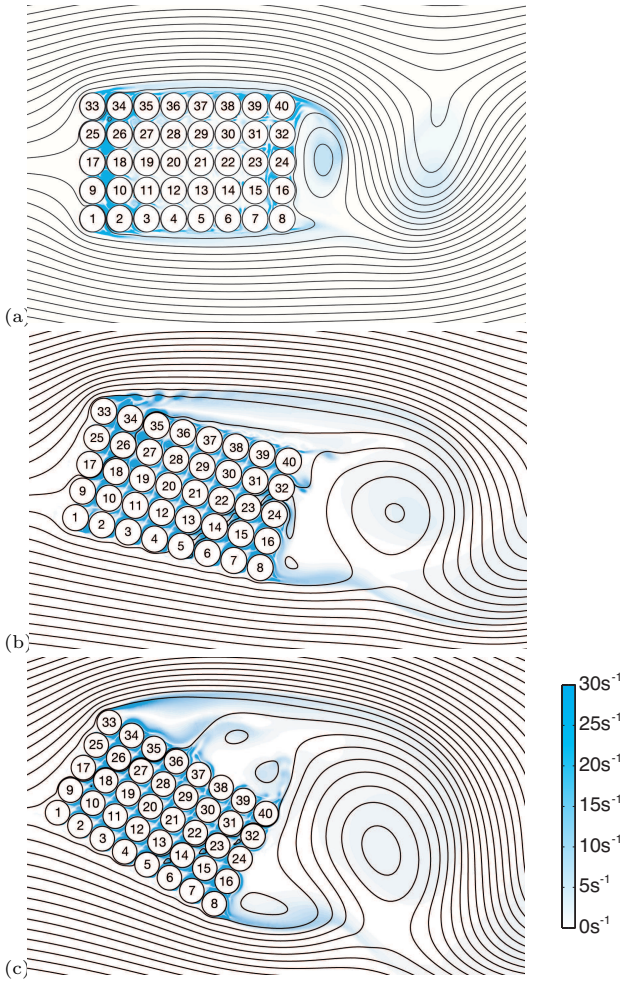

Figure 12: Velocity streamlines and vorticity contours (coloured) of the flow around the 8 by 5 cylinder group for an angle of incidence (a) $\alpha = 0°$ at $t = 80.0\,\mathrm{s}$, (b) $\alpha = 15°$ at $t = 82.5\,\mathrm{s}$, and (c) $\alpha = 30°$ at $t = 77.0\,\mathrm{s}$.

to the proximity of the separated shear layer. The same applies for the highest angles of incidence ($\alpha = 75°$ and $90°$), where no such recirculation zones can be formed on the lower side of the group (cylinders 8 to 40).

The flow around the group as a whole resembles the behaviour of a single bluff body in cross flow, similarly to what Kareem et al. [12] observed for two closely spaced cylinders in tandem arrangement. Comparison with experimental data of the flow around a bluff rectangular cylinder in cross flow might hence be useful to assess the influence of porosity and rounded corners of the present 8 by 5 silo group. However, no experimental data are available in literature for the present high Reynolds number. Knisely [13] performed experiments for a rectangular cylinder ($L/B = 1.67$) in cross flow, but at much lower Reynolds number ($1.2 \times 10^4 \leq \mathrm{Re} \leq 2.4 \times 10^4$). He found significantly lower Strouhal numbers (due to differences in Reynolds number and the rounded corners of the silo group), but also a sudden fall in Strouhal numbers for very small and very high angles of incidence ($\alpha \to 0°$ and $\alpha \to 90°$) when the separated shear layer reattaches to the cylinder surface. Since the emerging interstitial flows at the downstream side of the present group prevent the shear layer from reattaching, no such decrease of Strouhal numbers is observed in the present simulations.

α	[°]	0	15	30	45	60	75	90
D_g	[m]	28.7	38.4	45.9	50.6	52.3	50.7	46.1
f_{vs}	[Hz]	0.31	0.24	0.17	0.16	0.14	0.18	0.20
St		0.28	0.29	0.25	0.25	0.23	0.29	0.29

Table 7: Strouhal frequencies (f_{vs}) and Strouhal numbers (St) as a function of the angle of incidence (α) with respective projected width of the silo group (D_g).

3.4.2. The interstial flow in the cylinder group

The interstitial spaces of the present group configuration geometrically resemble those of tube bundles, which have been studied extensively for the design of heat exchangers. This does not imply, however, that identical physical phenomena will prevail in both cases as there are also important differences: the present group is limited to only 40 cylinders, the pitch between cylinders is much smaller than in heat exchangers and only 10% of the flow is passing through the interstitial spaces, while in heat exchangers all incident flow is forced through the interstitial spaces. A short account on differences and similarities is nevertheless interesting.

Tube bundles are typically divided in two categories [14]: the in-line category where cylinders are arranged in square or rectangle arrays and the interstitial flow is mostly straight through the arrays, and the staggered category where cylinders are arranged in rotated square or triangle arrays and the flow is forced along wavy paths. The in-line, square configuration could apply to the cases with $\alpha = 0°$ and $\alpha = 90°$ for the cylinder group while for all other angles of incidence the staggered, rotated square arrangement would be applicable. As shown in figure 13, this is not always the case.

No straight flow pattern for $\alpha = 0°$ (figure 13a) and $\alpha = 90°$ is found. For in-line tube bundles, the presence of the subsequent row prevents the transitional eddies to form and roll-up and the eddies are carried away between the tubes by the jet-like interstitial flow [15]. The present cylinders are too closely packed and these eddies are believed to partially or completely disappear in the distorted flow. Instead, the interstitial flow is not separated from the cylinder wall and follows a wavy path through the array, deflecting the flow up- and downward to the sides of the group, following the shortest path from the high pressures at the leading side of the group to the lower pressures at the lee side of the group. For other angles of incidence, interstitial flows resemble the wavy interstitial flow pattern of staggered tube bundles [14], e.g. for $\alpha = 30°$ (figure 13c). However, for $\alpha = 15°$ (figure 13b) and $\alpha = 60°$ (not shown), the regular wavy pattern is interrupted at arbitrary points in the array. Due to a fluctuating separation point on the cylinder surface at these locations, small recirculation zones are formed for $\alpha = 15°$ and even local vortex shedding arises inside the interstitial spaces for $\alpha = 60°$. These irregularities result in higher frequency components of the pressures in the interstitial spaces at respectively 2 Hz and 6 Hz.

4. Wind induced ovalling vibrations

Pressure distributions on the walls of the cylinders indicate whether wind induced vibrations of the silos can be excited. Both time averaged and fluctuating pressures should be considered seperately since they respectively provide an indication of the static and the dynamic deformations of the silo shell. The silos on the transverse upstream corners of the group where the shear layer is separated (e.g. cylinders 1 and 33 for $\alpha = 0°$, figure 12a, or cylinders 8 and 33 for $\alpha = 30°$, figure 12c) are subject to the largest static pressures for all angles of incident flow. The statically deformed silos at these locations may also be subject to observable rigid body motions due to the larger fluctuating drag forces (in two dimensions) at these corners. These vibrations are, however, fundamentally different from the observed ovalling shell vibrations of the silos.

Ovalling vibrations are triggered by the fluctuating pressures on the cylinder wall. Therefore, fluctuating pressure coefficients are determined as follows:

$$C_p'(\theta, t) = C_p(\theta, t) - \overline{C}_p(\theta) \tag{2}$$

To investigate the contribution of these fluctuating pressures in the excitation of the eigenmodes of the silos, the pressure coefficients are harmonically decomposed into a series of cosine functions with circumferential

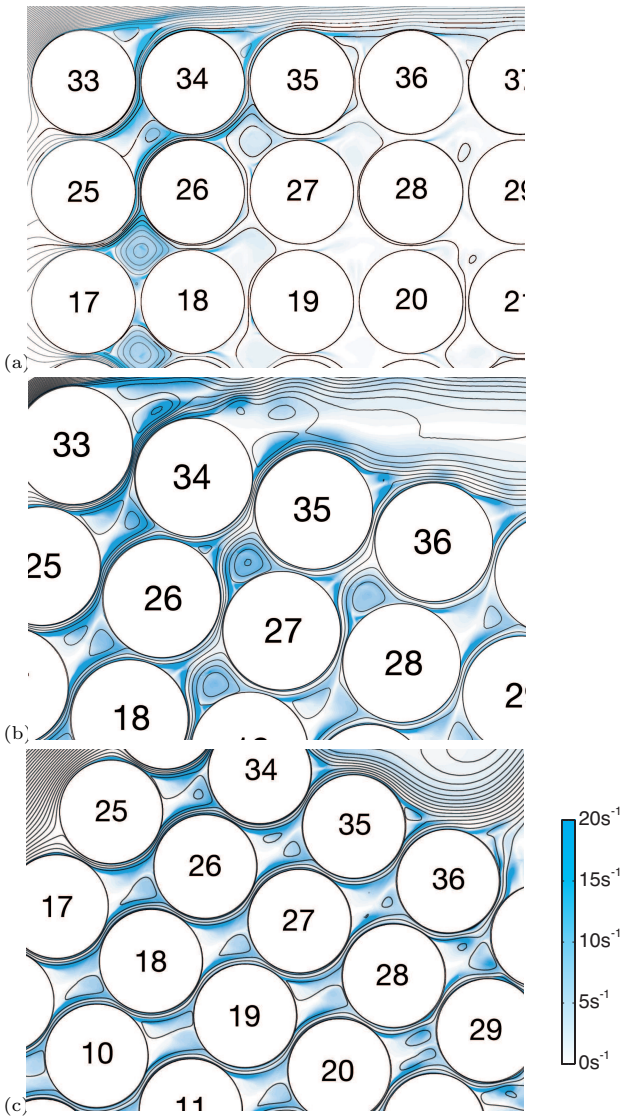

Figure 13: Detail of velocity streamlines and vorticity contours (coloured) for the interstitial space in the 8 by 5 cylinder group for an angle of incidence (a) $\alpha = 0°$ at $t = 78.5\,\mathrm{s}$, (b) $\alpha = 15°$ at $t = 77.0\,\mathrm{s}$, and (c) $\alpha = 30°$ at $t = 79.0\,\mathrm{s}$.

wavenumber n, corresponding to the ovalling mode shapes of the axisymmetric structure (figure 2):

$$C_{\mathrm{p}}'(\theta, t) = \sum_{n=0}^{\infty} C_{\mathrm{p}}'^{n}(t)\cos(n\theta + \overline{\phi}_n) \tag{3}$$

The time history of the fluctuating pressure amplitudes $C_{\mathrm{p}}'^{n}(t)$ is transformed to the frequency domain by means of a FFT algorithm afterwards, yielding $C_{\mathrm{p}}'^{n}(f)$. Wavenumber-frequency spectra of these amplitudes $C_{\mathrm{p}}'^{n}(f)$ for an angle of incidence $\alpha = 30°$ are shown in figure 14 for all cylinders.

It is observed that the contribution in the spectrum of the pressure fluctuations on the cylinder surfaces increases when moving downstream to the lee side of the group. At the same time, it is clear that the frequency contribution rapidly decreases as wavenumber n and frequency f increase, corresponding to measured wind spectra with typically low frequency components. This indicates that only structural mode

shapes with low natural frequencies f_n and a limited circumferential wavenumber n can possibly be excited by the dynamic wind pressures.

The wavenumber-frequency spectra $C_p'^n(f)$ at the upstream part of the group are dominated by low frequency contributions including the large vortex shedding in the wake of the group (table 7). However, following the wind towards the lee side of the group, irregularities appear, growing onwards to cylinder 40. In this part of the group, two clear higher frequency peaks can be observed between 3 Hz and 4 Hz and also at approximately 6.5 Hz. Taking into account the corresponding circumferential wavenumbers n on the vertical axis, it is concluded that the eigenmodes of the silos with three and four circumferential wavelengths $(1, 3)$ and $(1, 4)$ (figure 2), both at $f_n = 3.93$ Hz, might be excited by the dynamic wind pressures. Since the higher excitation frequency does not coincide exactly with any of the natural frequencies of the silos, higher eigenmode vibrations will always be less important.

For other angles of incidence, a similar analysis was performed and the peaks in the frequency range between 3 Hz and 4 Hz are also found. This confirms that the eigenmodes with the lowest eigenfrequencies, i.e. modes $(1, 3)$ and $(1, 4)$ (figure 2), will most likely be excited on the silos near the lee side corner of the silo group, depending on the angle of incidence of the wind. This also corresponds with the observed pattern of ovalling vibrations with three and four circumferential wavelengths on several silos near the lee side corner of the silo group in Antwerp during the 2002 storm.

Although it was shown that ovalling vibrations may be excited at the lee side corner silos of the group by linking the excitation by pressure fluctuations on the silo surfaces to the structural eigenmodes, the underlying mechanism inducing these vibrations has not yet been determined. It is generally accepted that there are three distinct mechanisms leading to vibrations in tube arrays [16, 17]. Firstly, forces can arise due to coincidence of a structural natural frequency with the vortex shedding frequency in the tube wake. Secondly, fluid-elastic instability (FEI) is based on self-excited forces which are caused by the interaction between tube motion and fluid flow [14]. Finally, turbulent buffeting forces arise due to turbulent fluctuations of the flow pressure, as a response to flow turbulence, either initiated upstream or induced within the array itself [16].

Considering the large difference between the natural ovalling frequencies (f_n, figure 2) and the vortex shedding frequencies (f_{vs}, table 7), resonance effects can be excluded as a mechanism inducing ovalling vibrations in the silo group. Although periodicities in the interstitial flow may be very different from classical vortex shedding (e.g. for $\alpha = 15°$), these do not seem to be related to ovalling either for two distinct reasons. Firstly, they occur throughout the entire group whereas ovalling is only observed on the corner silos and secondly, the higher frequencies of these interstitial periodicities do not coincide with any natural frequency of the silos. Hence, the ovalling vibrations seem to be caused by the unsteadiness in the flow but not due to vortex shedding, since other mechanisms as FEI and turbulent buffeting cannot be confirmed or excluded by this study. Further research is required to give a decisive explanation on these phenomena.

5. Conclusions

In order to elucidate the occurence of ovalling oscillations on the empty corner silos of a 8 by 5 silo group in the port of Antwerp, the post-critical flow around this closely spaced cylinder group was simulated numerically. 2D URANS simulations for the entire group were performed for 7 angles of incidence α between 0° and 90°.

For the verification of the computational procedure, various simulations have been performed, assessing inlet turbulence parameters, grid and time step refinement. It was found that imposing high turbulence intensities and similarly turbulence length scales at the inlet of the computational domain yields unphysical results in the URANS simulations. Validation was first performed for the better documented case of a single cylinder in cross flow. Afterwards, the simulations are also qualitatively validated by comparing the present flow with geometrically similar flows. While the rounded corners and the porosity of the silo group have an important influence, the flow regime around the group shows similarities with the fluid flow around bluff rectangular cylinders. Approximately 10% of the incident flow penetrates the group and emerges at the lee side, preventing the shear layer from reattaching at very low and high angles of incidence.

To verify whether ovalling vibrations can be excited, the transient pressure distributions on the silo surfaces in the group are linked to the dynamic structural properties of the silos. For all angles of incidence α, fluctuating pressures on the silos near the lee side corner of the group are seen to most likely excite the structural ovalling eigenmodes with three and four circumferential wavelengths, corresponding to the lowest natural frequencies of the silos. This observation is in agreement with the visually detected ovalling vibrations with three and four circumferential wavelengths of the silos near the lee side corner of the group in Antwerp during the 2002 storm. The ovalling vibrations seem to be caused by the unsteadiness in the flow while resonance with the vortex shedding frequency in separate tube wakes or the entire group wake can be excluded.

Acknowledgements

The results presented in this paper have been obtained within the frame of the FWO project G.0275.08 "Efficient analysis of fluid-structure interaction problems in structural dynamics", funded by the Research Foundation Flanders (FWO Vlaanderen). The second author is a post-doctoral fellow of the FWO. The support of FWO is gratefully acknowledged. We are grateful to the ICT Department of Ghent University for assistance with our computations.

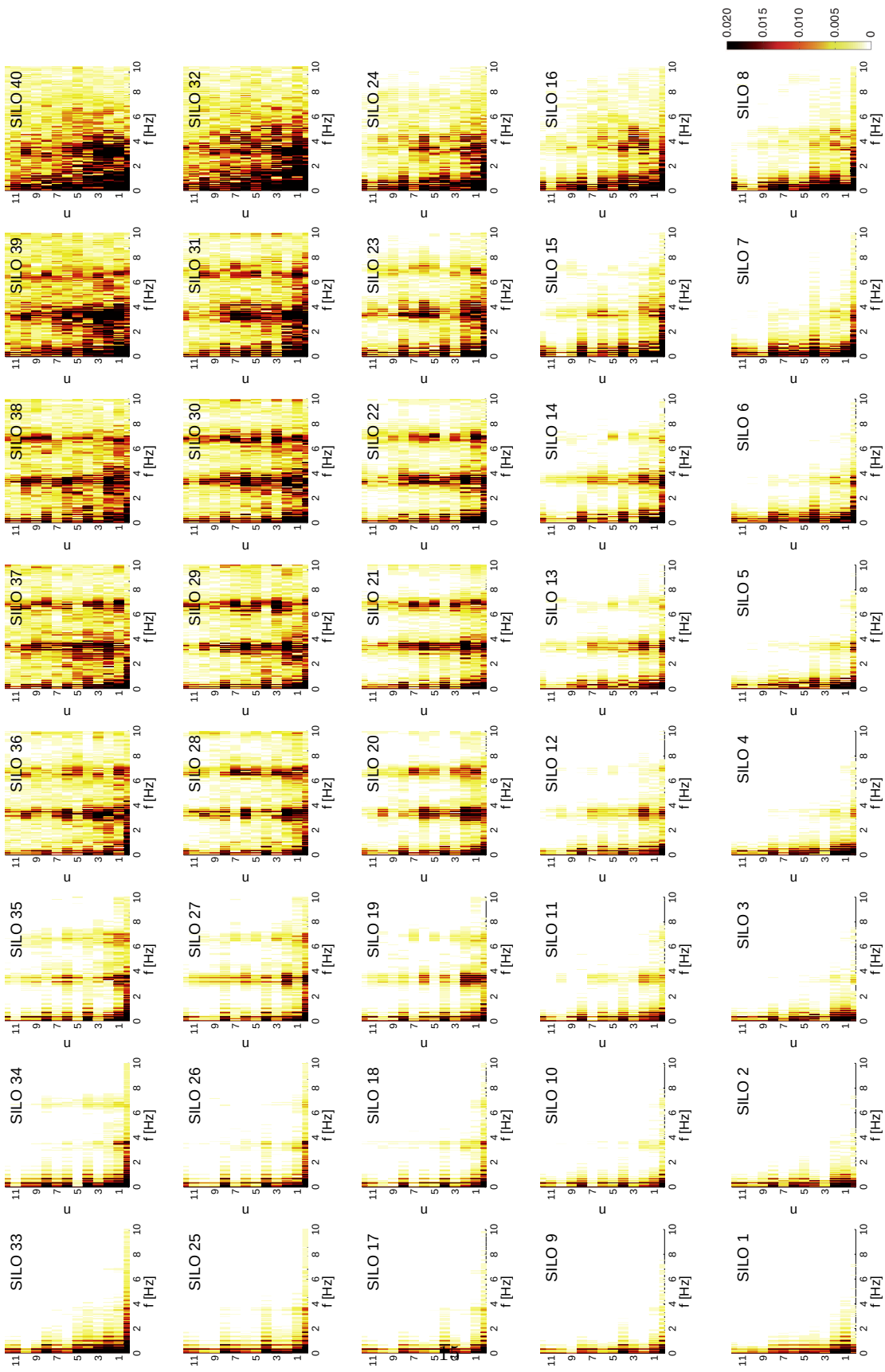

Figure 14: Wavenumber-frequency spectra of the amplitude $C_{\mathrm{p}}^{'n}(f)$ for angle of incidence $\alpha = 30°$.

References

[1] M.P. Païdoussis, S.J. Price, H.C. Suen, Ovalling oscillations of cantilevered and clamped-clamped cylindrical-shells in cross flow: An experimental-study, J. of Sound and Vibr. 83 (1982) 533–553.

[2] BIN, NBN EN 1991-1-4:2005 Eurocode 1: Actions on structures - Part 1-4: General actions - Wind actions, Belgisch Instituut voor Normalisatie, 2005.

[3] D. Dooms, G. Degrande, G. De Roeck, E. Reynders, Finite element modelling of a silo based on experimental modal analysis, Eng. Struct. 28 (2006) 532–542.

[4] ESDU, Data Item No. 85020: Characteristics of atmospheric turbulence near the ground. Part II: single point data for strong winds (neutral atmosphere), Engineering Science Data Unit, London, UK, 1985.

[5] H.K. Versteeg, W. Malalasekara, An Introduction to Computational Fluid Mechanics: The Finite Volume Method, Pearson Education Limited, Essex, England, second edition, 2007.

[6] W.C.L. Shih, C. Wang, D. Coles, A. Roshko, Experiments on flow past rough circular cylinders at large Reynolds numbers, J. of Wind Eng. and Ind. Aerodyn. 49 (1993) 351–368.

[7] M.M. Zdravkovich, Flow Around Circular Cylinders, Volume 1: Fundamentals, Oxford University Press, Oxford, England, 1997.

[8] S.J. Zan, Experiments on circular cylinders in crossflow at Reynolds numbers up to 7 million, J. of Wind Eng. and Ind. Aerodyn. 96 (2008) 880–886.

[9] G. Schewe, On the force-fluctuations acting on a circular-cylinder in cross-flow from subcritical up to transcritical Reynolds-numbers, J. of Fluid Mech. 133 (1983) 265–285.

[10] B.A. Younis, V.P. Przulj, Computation of turbulent vortex shedding, Comput. Mech. 37 (2006) 408–425.

[11] A. Travin, M. Shur, M. Strelets, P. Spalart, Detached-eddy simulations past a circular cylinder, Flow, Turb. and Combust. 63 (2000) 293–313.

[12] A. Kareem, T. Kijewski, P. Lu, Investigation of interference effects for a group of finite cylinders, J. of Wind Eng. and Ind. Aerodyn. 77–78 (1998) 503–520.

[13] C.W. Knisely, Strouhal numbers of rectangular cylinders at incidence: a review and new data, J. of Fluids and Struct. 4 (1990) 371–393.

[14] M.M. Zdravkovich, Flow Around Circular Cylinders, Volume 2: Applications, Oxford University Press, Oxford, England, 2003.

[15] J.C.R. Hunt, I. Eames, The disappearance of laminar and turbulent wakes in complex flows, J. of Fluid Mech. 457 (2002) 111–132.

[16] S.J. Price, M.P. Païdoussis, R. Macdonald, B. Mark, The flow-induced vibration of a single flexible cylinder in a rotated square array of rigid cylinders with a pitch-to-diameter ratio of 2.12, J. of Fluids and Struct. 1 (1987) 359–378.

[17] D.S. Weaver, H.Y. Lian, X.Y. Huang, Vortex shedding in rotated square arrays, J. of Fluids and Struct. 7 (1993) 107–121.